A&A 475, 71–81 (2007)
DOI: 10.1051/0004-6361:20078015

Astronomy & Astrophysics

The importance of merging activity for the kinetic polarization of the Sunyaev-Zel'dovich signal from galaxy clusters

M. Maturi[1], L. Moscardini[2,3], P. Mazzotta[4,5], K. Dolag[6], and G. Tormen[7]

[1] Zentrum für Astronomie, ITA, Universität Heidelberg, Albert-Überle-Str. 2, 69120 Heidelberg, Germany
[2] Dipartimento di Astronomia, Università di Bologna, via Ranzani 1, 40127 Bologna, Italy
[3] INFN – National Institute for Nuclear Physics, Sezione di Bologna, viale Berti Pichat 6/2, 40127 Bologna, Italy
[4] Dipartimento di Fisica, Università di Roma Tor Vergata, via della Ricerca Scientifica 1, 00133 Roma, Italy
[5] Harvard-Smithsonian Center for Astrophysics, 60 Garden Street, Cambridge, MA 02138, USA
[6] Max-Planck Institute fuer Astrophyik, Karl-Schwarzschild Strasse 1, 85748 Garching, Germany
[7] Dipartimento di Astronomia, Università di Padova, vicolo dell'Osservatorio 2, 35122 Padova, Italy

Receievd 5 June 2007 / Accepted 13 July 2007

ABSTRACT

Context. The polarization sensitivity of upcoming millimetric observatories will open new possibilities for studying the properties of galaxy clusters and for using them as powerful cosmological probes. For this reason it is necessary to investigate in detail the characteristics of the polarization signals produced by their highly ionized intra-cluster medium (ICM). This work is focused on the polarization effect induced by the ICM bulk motion, the so-called kpSZ signal, which has an amplitude proportional to the optical depth and to the square of the tangential velocity.
Aims. We study how this polarization signal is affected by the internal dynamics of galaxy clusters and its dependence on the physical modelling adopted to describe the baryonic component.
Methods. This is done by producing realistic kpSZ maps starting from the outputs of two different sets of high-resolution hydrodynamical N-body simulations. The first set (17 objects) follows only non-radiative hydrodynamics, while for each of 9 objects of the second set we implement four different kinds of physical processes.
Results. Our results shows that the kpSZ signal is a very sensitive probe of the dynamical status of galaxy clusters. We find that major merger events can amplify the signal up to one order of magnitude with respect to relaxed clusters, reaching amplitudes up to about 100 nK. This result implies that the internal ICM dynamics must be taken into account when evaluating this signal because simplicistic models, based on spherical rigid bodies, may provide wrong estimates. In particular, the selection of sufficient relaxed clusters seems to be fundamental to obtain a robust measurement of the intrinsic quadrupole of the cosmic microwave background through polarization. We find that the dependence on the physical modelling of the baryonic component is relevant only in the very inner regions of clusters.

Key words. polarization – cosmic microwave background – galaxies: clusters: general – cosmology: theory – methods: numerical

1. Introduction

The lastest generation of X-ray satellites like Chandra and XMM-Newton have revealed a complex scenario for the intra-cluster medium (ICM). In particular the presence of cold fronts has been detected in many galaxy clusters (see, e.g., Allen et al. 2001). The existence of this phenomenon suggests that relaxed clusters behave unlike the previously hypothesized hydrostatic state for the ICM, showing minor merger events and evident gas motion.

In this paper we focus on a different signal that could place strong constraints on the merging activity of galaxy clusters: the kinematic Sunyaev-Zel'dovich (SZ) polarization (hereafter kpSZ) (Sunyaev & Zel'dovich 1980b). It originates in single scattering of moving electrons, and its dependence on the square of their tangential velocity makes it a suitable probe for investigating the dynamic properties of clusters during the non-linear process of their formation.

As we will discuss in more detail in Sect. 2, galaxy clusters produce other linear polarization contributions to the cosmic microwave background (CMB) radiation through different processes (see, e.g., Sazonov & Sunyaev 1999). All components of the quadrupole moment present in the incoming radiation induce a linear polarization: there is the polarization induced by the intrinsic quadrupole of the CMB radiation ($P_{\rm Q}$), by the quadrupole component of kinetic and thermal SZ effects ($P_{\rm kp^2SZ}$ and $P_{\rm tp^2SZ}$, respectively) and by the gravitational lensing effect ($P_{\rm l}$) of clusters themselves. These polarization contributions, with the exception of $P_{\rm kp^2SZ}$, which is one order of magnitude smaller, have amplitudes similar to the kpSZ effect (Lavaux et al. 2004). Thus, none of them can be neglected. A component separation is possible, thanks to their different frequency dependences. Each of these signals carries different and important information on galaxy clusters and cosmology. For example, $P_{\rm Q}$ could be used to estimate the intrinsic quadrupole at different redshift and thus to investigate the dark energy evolution; $P_{\rm tp^2SZ}$ can be used to constrain the gas profile thanks to its dependence on the square of the gas density; $P_{\rm kpSZ}$, which we discuss in this paper, is a tool to study the ICM dynamics and thus the history of the merging activity.

Using a toy-model, Diego et al. (2003) showed that the kpSZ effect strongly depends on sub-clump motions, and that major merger events could make this signal equal to or dominant over the other ones (depending on the assumed frequency).

A different study based on a numerical simulation has been carried out by Lavaux et al. (2004), who looked at their attention on the large scale structure of the kpSZ signal. Their results show that the environmental collapse into the potential of the forming cluster generatesa characteristic kpSZ pattern with circular symmetry. They suggested to use this peculiar pattern to detect forming clusters. In addition they confirmed the analytic results of Sazonov & Sunyaev (1999), but they did not investigate the dependence of this signal on the merging activity of the clusters and they did not perform any extended statistical study. Shimon et al. (2006), using a cluster simulated by the *ENZO* code, investigated the polarization levels and patterns produced by the different components originated by the kinematic quadrupole moments induced by moving scattering electrons: their conclusion is that the signal is high enough ($\approx 1\ \mu$K) to be detectable in upcoming CMB experiments.

Here we extend these works by analyzing two different sets of high-resolution hydrodynamical N-body numerical simulations, assuming different modeling for the ICM physics, to investigate the statistical properties of the kpSZ signal. We demonstrate that it can vary up to one order of magnitude depending on the internal cluster dynamics.

In Sect. 2 we introduce the Stokes parameters and the primary polarization of the CMB, then we present the main polarization contributions induced by galaxy clusters, discussing in more detail the kpSZ polarization. Section 3 is devoted to an extended description of the two sets of numerical hydrodynamical simulations used for our analysis. Section 4 introduces two examples of galaxy clusters, a relaxed cluster participating in a major merger, and a dynamically more active object: the corresponding signals are compared to investigate the influence of the in-falling haloes on the kpSZ signal. The statistical analysis of the full samples of simulated objects is presented in Sect. 5, where we consider the results of non-radiative simulations and the ones obtained including different ICM modeling. Our main conclusions are summarized in Sect. 6.

2. Linear polarization by scattering with free electrons

Scattering by free electrons induces a linear polarization component only if the incoming radiation has a quadrupole anisotropy. In the case of the CMB photons, we can distinguish different polarization components according to the origin of the quadrupole moment of the incoming radiation and to the location of the free electrons. In this section we briefly review these processes.

2.1. Parametrizing polarization

Radiation can be parametrized by using the four Stokes parameters: I represents the total intensity of the light, Q and U quantify the degree of linear polarization, while V gives the degree of circular polarization. Since the Thompson scattering does not introduce any circular polarization, we can set $V = 0$ here. Notice that polarization is a pseudo-vector, whose orientation is given by

$$\chi = \frac{1}{2}\tan^{-1}\left(\frac{U}{Q}\right). \tag{1}$$

The degree of polarization p can be expressed as

$$p = \frac{\sqrt{Q^2 + U^2}}{I}. \tag{2}$$

The Stokes parameters are additive along the line-of-sight, and thus the total effect can be computed as the integral of local effects: $Q = \int \mathrm{d}Q$ and $U = \int \mathrm{d}U$.

Throughout this paper, we compute the polarization effect assuming the incoming CMB radiation to be unaffected by the SZ effect, i.e. $I \simeq I_{\rm CMB}$: this is justified by the assumption of low optical depth.

2.2. Primary CMB polarization

The CMB has a primordial polarization component origining at the last scattering surface. At that epoch, the universe was fully ionized and the quadrupole moment was related to the primary anisotropies. This signal is expected to peak inside the cosmological horizon scale at that time, because it is a causal process requiring a coherence in the electron motion. This polarization signal has been recently measured by the WMAP satellite, which also detected a large-scale component $l(l+1)C^{\rm EE}_{l=\langle 2-6\rangle}/2\pi = 0.086 \pm 0.029\ \mu\mathrm{K}^2$, interpreted as a signature of a global reionization that occurred at redshift $z = 10.9^{+2.7}_{-2.3}$ (Page et al. 2007).

2.3. Secondary CMB polarization by galaxy clusters

Free electrons are also present in the ICM of galaxy clusters. In this case the polarization components depend on the nature of the quadrupole moment of the incoming radiation, as we discuss in the following subsections.

2.3.1. Polarization by single scattering of moving electrons: *pkSZ*

Our work is focused on the kpSZ effect discussed here. This effect arises from single scattering of the CMB photons by the ICM electrons. A moving electron sees the CMB radiation as Doppler-shifted because of its peculiar motion and thus perceives a radiation intensity given by

$$I(\nu,\mu) = \frac{Cx^3}{\mathrm{e}^{x\gamma(1+\beta\mu)} - 1}, \tag{3}$$

where $x \equiv h\nu/(kT)$ is the adimensional frequency, $\beta \equiv v_{\rm e}/c$ gives the electron velocity in units of the speed of light, $\gamma \equiv (1-\beta^2)^{-1/2}$ is the Lorentz factor, μ is the cosine of the angle between the direction of the electron velocity and that of the incident CMB photon. The decomposition of this function into Legendre polynomials leads to

$$I(\nu,\mu) = \frac{Cx^3}{\mathrm{e}^x - 1}\left[I_0 + I_1\mu + I_2\left(\mu^2 - \frac{1}{3}\right)\frac{\mathrm{e}^x(\mathrm{e}^x+1)}{2(\mathrm{e}^x-1)^2}x^2\beta^2 + ...\right]. \tag{4}$$

The previous equation contains the quadrupole component necessary to produce a linear polarization orthogonal to the electron velocity direction (Sunyaev & Zel'dovich 1980a; Sazonov & Sunyaev 1999).

The resulting local contributions to the Q and U Stokes parameters are

$$\begin{aligned} \mathrm{d}Q &= -0.1\sigma_{\rm T} n_{\rm e} f(x)\beta_{\rm t}^2 \cos(2\chi)\mathrm{d}l \\ \mathrm{d}U &= -0.1\sigma_{\rm T} n_{\rm e} f(x)\beta_{\rm t}^2 \sin(2\chi)\mathrm{d}l, \end{aligned} \tag{5}$$

respectively. In the previous equation, $\sigma_{\rm T}$ represents the Thompson cross-section, $n_{\rm e}$ is the electron density, $\beta_{\rm t}$ is the component of $\boldsymbol{\beta}$ on the sky plane (tangential velocity), χ defines the position angle of the tangential velocity, and

$$f(x) = \frac{\mathrm{e}^x(\mathrm{e}^x+1)}{2(\mathrm{e}^x-1)^2}x^2 \tag{6}$$

is the non-relativistic approximation of the frequency dependence of the polarization signal, as results of the quadrupole component of Eq. (4). The Stokes parameters (see Eq. (5)) are normalized by the incoming mean intensity of the CMB radiation and are referred to the observer rest frame. They can be converted into a brightness temperature by dividing the previous quantities by

$$g(x) = \frac{\mathrm{d}\ \ln I_\nu}{\mathrm{d}\ \ln T} = \frac{x\mathrm{e}^x}{\mathrm{e}^x - 1}. \quad (7)$$

Equation (5) shows the kpSZ effect dependence on the square of the tangential velocity β_t^2 and on its direction χ. Therefore this effect is very sensitive to the ICM dynamics and its amplitude can be used to investigate the merging activity.

2.3.2. Polarization by single scattering of the intrinsic CMB quadrupole: P_Q

The CMB radiation has an intrinsic quadrupole moment given by the Sachs-Wolfe effect and by the late Integrated Sachs-Wolfe effect, which is mostly related to the presence of a dark energy component. This polarization component depends on the optical depth τ and on the amplitude of the quadrupole $Q(z)$ at the cluster redshift where the scattering process occurs: $P_Q \propto \tau Q(z)$.

Because of that, if we have an estimate of τ, for example from SZ measurements, we can evaluate the intrinsic quadrupole of the CMB at different redshifts. For a flat ΛCDM model with $\Omega_\Lambda = 0.7$, the maximum signal is of the order of 4.9τ μK. Assuming a typical value of $\tau \sim 0.03$, this leads to a maximum signal of $\sim 0.14\,\mu$K, as found analytically by Sazonov & Sunyaev (1999). This result has been confirmed by the numerical simulations performed by Amblard & White (2005). A more detailed study of the primordial CMB quadrupole-induced polarization based on the combination of an analytic method with hydrodynamic simulations has been carried out by Liu et al. (2005), who also investigated the contributions to the signal of different gas phases. Because of the dependence on Q, there are four orthogonal regions in the sky where P_Q vanishes or at least is very low. These regions have been located by the WMAP satellite: one of them is at galactic coordinate $(l, b) \approx (-80°, 60°)$, close to the Virgo cluster (Tegmark et al. 2003).

This observable is one of the most sensitive probes of the dark energy: infact the growth of the gravitational potential, and thus of Q, is directly proportional to its equation of state. On the contrary all other related quantities depend at least on an integral of this quantity.

2.3.3. Polarization by second scattering of the tSZ and kSZ quadrupoles: P_{p^2tSZ}, P_{p^2kSZ}

A first Thompson scattering of the CMB radiation with the ICM electrons introduces two secondary anisotropies, called kinetic and thermal Sunyaev Zel'dovich effects. They have a quadrupole component and thus a second scattering would generate a linear polarization related to each of them. We call P_{p^2tSZ} and P_{p^2kSZ} the polarization signals induced by the tSZ and kSZ effects, respectively. As shown by Sunyaev & Zel'dovich (1980a), these polarization contributions depend only on the local density of free electrons and not on their temperature. The corresponding amplitudes are proportional to the square of the optical depth τ^2, because of the two scattering events involved in the process (Sazonov & Sunyaev 1999); consequently they are very sensitive probes of the gas profile. The P_{p^2kSZ} is one order of magnitude stronger than the P_{p^2tSZ}, which can be even larger than the P_Q signal, depending on the considered frequency (Lavaux et al. 2004).

2.4. Possible contaminants

Many other processes can introduce significant contributions to the linear polarization, like the Galactic synchrotron emission by our Galaxy and by point radio sources, and the scattering on Galactic dust grains. In general these processes have different frequency dependences, allowing their separation through multi-band observations, similarly to the techniques adopted for the CMB temperature maps (see, e.g., Tegmark et al. 2000). The component-separation method could also be improved by including in the foreground subtraction our knowledge of the distributions of dust, gas and magnetic fields in the Galaxy. In particular, if one is mostly interested in the polarization contributed of galaxy clusters, the observations could be focused in regions at high galactic latitudes, where the foreground effect is minimal. Also the polarization induced by the CMB quadrupole (P_Q) and that induced by the thermal SZ effect (P_{p^2tSZ}) have a different frequency dependence, favoring their separation. In addition P_Q has typical scales larger than the kpSZ signal, so that the use of optimal spatial filters (see, e.g., Hu 2001; Maturi et al. 2005) could drastically reduce its contamination.

The magnetic fields, combined with the presence of free electrons in galaxy clusters, may cause a Faraday rotation of the polarization orientation, reducing its magnitude. This rotation angle is relatively small even for massive galaxy clusters: $\Delta_{RM} \simeq 1{-}10°\,(10\ \mathrm{GHz}/\nu)^2$ (Ohno et al. 2003), however it could become significant when considering our Galaxy at low galactic latitudes (see, e.g., Burigana et al. 2006).

It is well known that a polarization signal is also produced by both the reionization process (see, e.g., Ng & Ng 1996) and weak gravitational lensing (see, e.g., Zaldarriaga & Seljak 1998). In particular, the deflection of the CMB photons leads to a smoothing of the small-scale features and to a power enhancement of the damping tail in the power spectrum. The analysis of the weak lensing effect on the CMB has been suggested as a possible tool to reconstruct cluster mass (Hu et al. 2007): in this case the kpSZ signal represents a possible source of noise which must be considered to avoid systematic effects.

3. Numerical simulations

We use two different sets of resimulated galaxy clusters. Both have been extracted from a dark matter(DM)-only simulation (see Yoshida et al. 2001) of a "concordance" flat ΛCDM model, where the contributions to the density parameter from matter and the cosmological constant are $\Omega_{0m} = 0.3$ and $\Omega_{0\Lambda} = 0.7$ respectively; the Hubble constant in units of 100 km s^{-1} Mpc^{-1} is $h = 0.7$. The initial conditions of the parent simulation that followed the evolution of 512^3 particles with mass of $6.86{\times}10^{10}\,h^{-1}\,M_\odot$ in a comoving cubic box of $479\,h^{-1}$ Mpc per side were set considering a cold dark matter power spectrum normalized by assuming $\sigma_8 = 0.9$.

In the catalogue of haloes identified in the final output of the parent simulation by adopting a spherical overdensity criterion, we selected some objects to be re-simulated with higher mass and force resolution The new initial conditions were created by using the "Zoomed Initial Conditions" (ZIC) technique (Tormen et al. 1997). This method identifies in the initial domain the Lagrangian region corresponding to each cluster up to few virial radii and populates it with more particles (of both

DM and gas), properly adding small-scale modes. At the same time the volume outside the region of interest is sampled by low-resolution particles which allow us to reproduce the original tidal effects of the cosmological environment.

The new re-simulations, starting at redshift $z_{\rm in}$ ranging between 35 and 60, have been carried out using for the first sample the Tree-Smoothed Particle Hydrodynamics (SPH) parallel code GADGET (Springel et al. 2001), while for the second set we ran its new version GADGET-2 (Springel 2005), which includes an entropy-conserving formulation of SPH (Springel & Hernquist 2002) and allows the treatment of many physical processes affecting the baryonic component (see below). The gravitational softening length was kept fixed at $30\,h^{-1}$ kpc comoving (Plummer-equivalent) for $z > 5$, and was switched to a physical softening length of $5\,h^{-1}$ kpc at smaller redshifts.

The first sample is comprised of 17 randomly selected galaxy clusters, whose structure and dynamical properties have been discussed in Rasia et al. (2004) and Tormen et al. (2004), respectively. These simulations, which follow only non-radiative hydrodynamics, assume a baryonic density corresponding to $\Omega_{0\rm b} = 0.03$; the particle masses in the high-resolution region range from $2 \times 10^9\,h^{-1}\,M_\odot$ to $6 \times 10^9\,h^{-1}\,M_\odot$ for DM, and from $3 \times 10^8\,h^{-1}\,M_\odot$ to $7 \times 10^8\,h^{-1}\,M_\odot$ for gas. The final objects have virial masses between $3.1 \times 10^{14}\,h^{-1}\,M_\odot$ and $1.7 \times 10^{15}\,h^{-1}\,M_\odot$, and virial radii[1] between 1.4 and $2.5\,h^{-1}$ Mpc.

The second sample is comprised of 9 more isolated objects, 4 of them with the typical size of clusters (about $10^{15}\,h^{-1}M_\odot$), and 5 of group-like systems (about $10^{14}\,h^{-1}\,M_\odot$). In this case the baryonic density has been fixed to $\Omega_{0\rm b} = 0.04$. Each cluster of this set has been re-simulated 4 times, turning on different kinds of physical processes:

1. gravitational heating only with an ordinary treatment of gas viscosity (hereafter the *ovisc* model);
2. like *ovisc*, but using an alternative implementation of the artificial viscosity (hereafter the *lvisc* model), which allows us to better resolve the turbulence driven by fluid instabilities; this leads to a non-negligible contribution of non-thermal pressure support in the central region of galaxy clusters (Dolag et al. 2005);
3. cooling, star formation and supernovae feedback with weak galactic winds, having a speed of ∼340 $\rm km\,s^{-1}$ (the *csf* model);
4. like *csf*, also including thermal conduction (see Jubelgas et al. 2004; Dolag et al. 2004), where the isotropic effective conductivity is fixed to 1/3 of the Spitzer rate (the *csfc* model).

A more detailed presentation of the properties of the clusters of this second set can be found elsewhere (see, e.g., Ettori et al. 2006; Roncarelli et al. 2006).

The simulated clusters of the first sample have been randomly chosen from the complete list of haloes identified at $z = 0$ in the parent simulation, with the only requirement of sampling in a sufficiently complete way the mass range above $10^{14}\,h^{-1}\,M_\odot$. For this reason they have varying dynamical and environmental properties, comprising relaxed and non-relaxed objects, isolated and interacting systems. This allows us to consider this sample as representative of the whole population of galaxy clusters. On the other hand, the clusters of the second set have been chosen to be more isolated structures, so that their main properties are not affected by recent major merger events and thus the effects of the four different ICM models can be better identified.

To compute the final Stokes parameters related to the kpSZ signal, we need to integrate Eq. (5) along the line-of-sight. This is done by considering boxes of $(8\,\rm Mpc)^3$ centered on the cluster: the resulting maps have a resolution of 15.6 kpc. The polarization contributed by each particle, or moving cloud, adds constructively if their tangential velocities have the same orientation, even if they have opposite direction. On the other hand, if their tangential velocities are orthogonal, the polarization tends to cancel. Because of that, only the coherent motion of gas clouds produces a polarization contribution, unlike the thermal motion of electrons, which is randomly oriented and does not contribute to the signal.

4. The importance of the merging activity

4.1. Two examples with different dynamical state

To discuss the role of the merging activity, we analyzed two clusters of our first sample, g24+200 and g7. The first object represents a relaxed halo falling with high velocity into the potential well of another cluster. Consequently the velocity field of its gas is dominated by the bulk motion of the whole system. For this reason it can be considered at the same time as an example of a relaxed halo and of a major merger event because of its bulk motion given by the companion cluster. Conversely, the second object is not relaxed and is acquiring new matter from different in-falling subclumps having high velocities.

Figure 1 shows a region of $8\times8\,\rm Mpc^2$ centered on cluster g7. This object has a virial mass of $1.46 \times 10^{15}\,h^{-1}\,M_\odot$ and a virial radius of $2.35\,h^{-1}$ Mpc (indicated by the circle in the plots). In the upper-left panel we overlay the mass-weighted tangential velocity field of the gas on its density iso-contours (red curves); the arrow length is proportional to the velocity. The upper right panel shows the corresponding map for the mass-weighted temperature of the gas; the color scale is given in the upper part of the panel. In the bottom left panel we show the polarization pseudo-vector field, where the lengths of the lines are proportional to the polarization amplitude. The lines sample the signal on a grid having a lower resolution, giving only an idea of the polarization and velocity directions. We draw in the bottom-right panel the amplitude of the polarization signal using a logarithmic scale (reported in the upper part). The polarization maps are computed at a frequency of 300 GHz.

Since the polarization is proportional to the projected density and to the squared tangential velocity (see Eq. (5)), the signal peaks in the core of the merging haloes, where the column density of electrons and the tangential bulk motion are large. The kpSZ signal of some in-falling blobs can be even stronger than the cluster core itself: an example is the blob approximately located at the position (0.5 Mpc , 3.0 Mpc).

In Fig. 2 we display the same quantities for the cluster g24+200, which has a virial mass of $6.54 \times 10^{14}\,h^{-1}M_\odot$ and a virial radius of $1.80\,h^{-1}$ Mpc. Unlike cluster g7, for this object the polarization inside the virial radius is dominated by the cluster core where the signal shows a constant direction. Outside the virial radius there are two more evident structures which do not belong to this cluster: the first one is a small but rapidly infalling blob, the second one, located at the position (3.8 Mpc, 2.4 Mpc), represents a different cluster. The absolute value of the polarization signal of this cluster is large because it is taking part in a major merger event: it is moving with a bulk velocity

[1] Virial radii are defined using the overdensity threshold dictated by the spherical top-hat model (see, e.g., Eke et al. 1996).

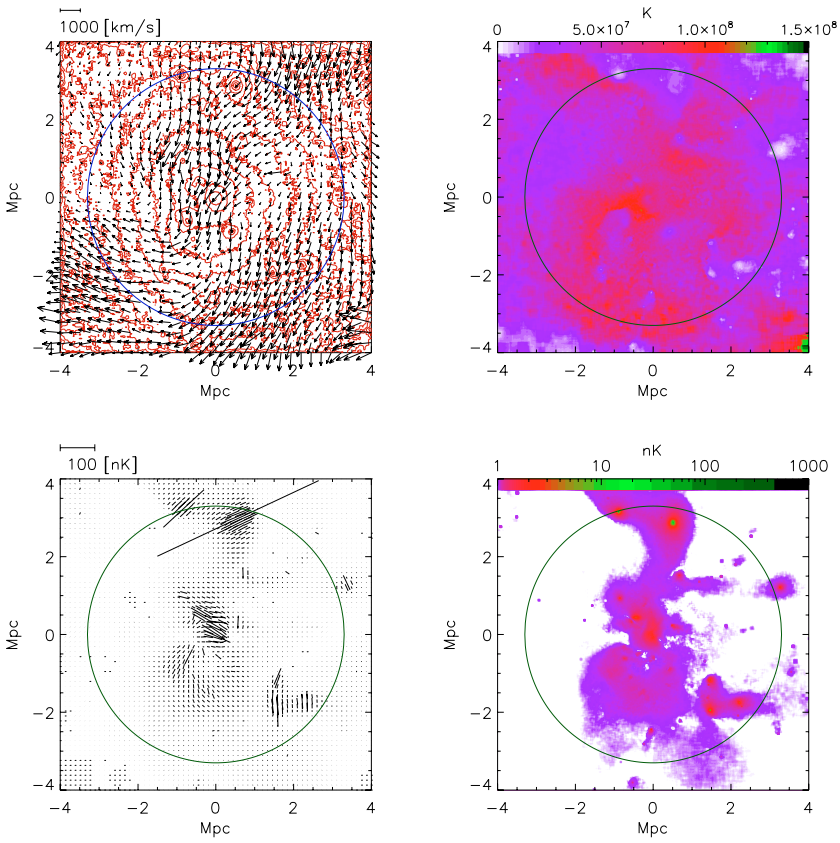

Fig. 1. Maps of a region of $8 \times 8\,\mathrm{Mpc}^2$ centered on the simulated cluster g7. *Upper left panel*: arrows represent the (mass-weighted) tangential velocity of the gas; the overlaid levels refer to the density iso-contours. *Upper right panel*: the gas (mass-weighted) temperature. *Bottom left panel*: the direction of the polarization pseudo-vector field. *Bottom right panel*: the polarized radiation amplitude. The different scale units or color levels are shown above the corresponding panels. In all panels, the circle indicates the virial radius.

of $1200\,\mathrm{km\,s^{-1}}$ in the direction of the other cluster visible in this field.

We discuss the differences between these two clusters and the importance of their merging activity in the following subsections.

4.2. Excluding the merging activity

In order to better understand the influence of the merging activity on the polarization signal, we compare the polarization map displayed in Figs. 1 and 2 with the ones obtained by artificially "freezing" the internal dynamics. This is done by associating the mean bulk velocity[2] of the whole cluster to all particles inside the box, so that the cluster moves like a rigid body. For simplicity we will refer to these simulations as *"merging-free"*.

The top panels in Fig. 3 show the polarization signal obtained in such a way for the unrelaxed cluster g7 (on the left) and for the relaxed cluster g24+200 (on the right). The polarization signal is proportional to the length of the lines and it is displayed using the same scale adopted for Figs. 1 and 2. On the top of these panels, we show an arrow corresponding to the bulk velocity of each galaxy cluster. The iso-polarization contours in the upper panels start from 1 nK and show power of 2 steps, i.e 2, 4, 8, 16 nK, etc. Note that the large structure in the upper-right corner of the g24+200 panel is an artifact due to the procedure performed to obtain the "merging-free" simulation. In fact, the bulk motion of the cluster could be assigned only to the particles inside the virial radius. Consequently, in the "merging-free" simulations only the region inside the virial radius has a physical meaning and will be considered in the following discussion.

[2] In order to avoid the contamination given by in-falling blobs, this is defined as the velocity associated with the baricentre of the most inner 50 per cent of the cluster mass.

4.3. Quantifying the merging

As described above, we computed the kpSZ signal of our two clusters, considering both the real simulations and the "merging-free" versions of them. Comparing the corresponding results, we can evaluate the amplification of the polarization signal produced by the merging activity. This is done by computing the per cent increment of the signal, defined as

$$\Delta(\boldsymbol{\theta}) \equiv \frac{P(\boldsymbol{\theta}) - P_{\rm mf}(\boldsymbol{\theta})}{P_{\rm mf}(\boldsymbol{\theta})}, \tag{8}$$

where P and $P_{\rm mf}$ are the polarization signals given by the real and "merging-free" simulations, respectively. A map of this quantity is shown for both clusters in the bottom panels of Fig. 3. Clearly the relaxed cluster in the left panel strongly differs from the non-relaxed object in the right panel. In the first case (g24+200) there is only a small increment of the signal (30 per cent at most) and only over a small area centered on a small halo; the signal of the cluster core is substantially unchanged, showing an increment by only 10 per cent. In the second case (cluster g7) a large fraction of the object shows a substantial signal increment, especially in the outer regions, where most of the in-falling blobs are located. Here the merging activity produces an increment by 170 per cent in the cluster core and up to a factor of 10 at the positions of five different sub-halos, three of which have a signal even stronger than the cluster core itself.

To better describe the distribution of the polarization, in Fig. 4 we report the fraction of the virial area covered by the galaxy clusters where the signal is larger than a given threshold. The results for the merging cluster g7 and for the relaxed system g24+200 are shown in the upper and bottom panels, respectively; in this case all three orthogonal projections have been considered. The solid lines refer to the original

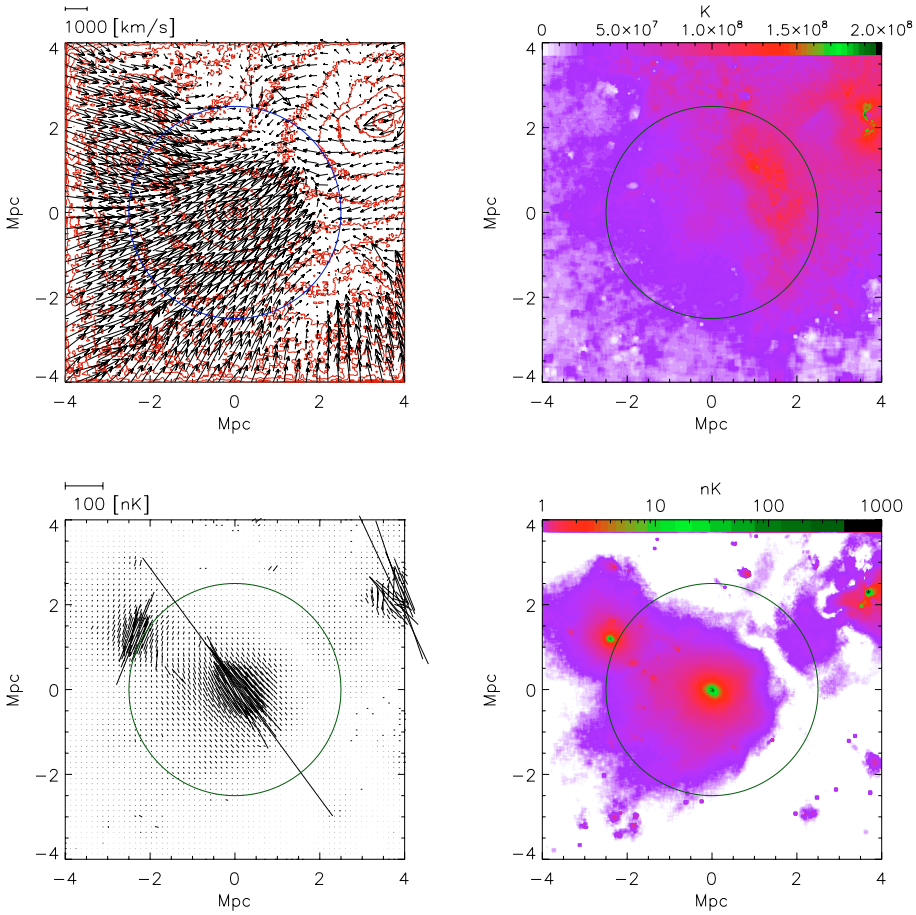

Fig. 2. As Fig. 1, but for the simulated galaxy cluster g24+200.

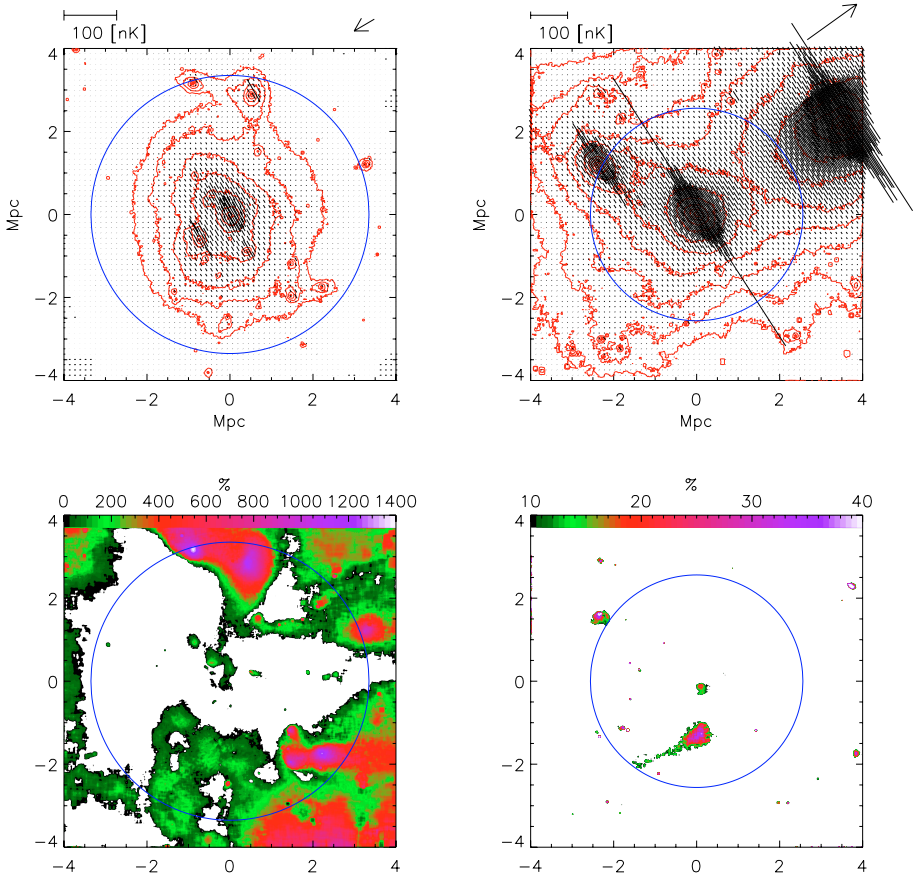

Fig. 3. Comparison with "merging-free" simulations. Left and right panels refer to the dynamically active cluster g7 and to the more relaxed cluster g24+200, respectively. *Top panels*: the polarization signal obtained from the "merging-free" simulations, shown by adopting the same scales and units of Figs. 1 and 2. The iso-polarization contours start from 1 nK and show power of 2 steps. An arrow proportional to the bulk velocity of each cluster and its direction is displayed in the top right. *Bottom panels*: maps for the per cent increment of the polarization signal, given by the merging activity, as expressed by Eq. (8). The corresponding color scale is shown above the panels.

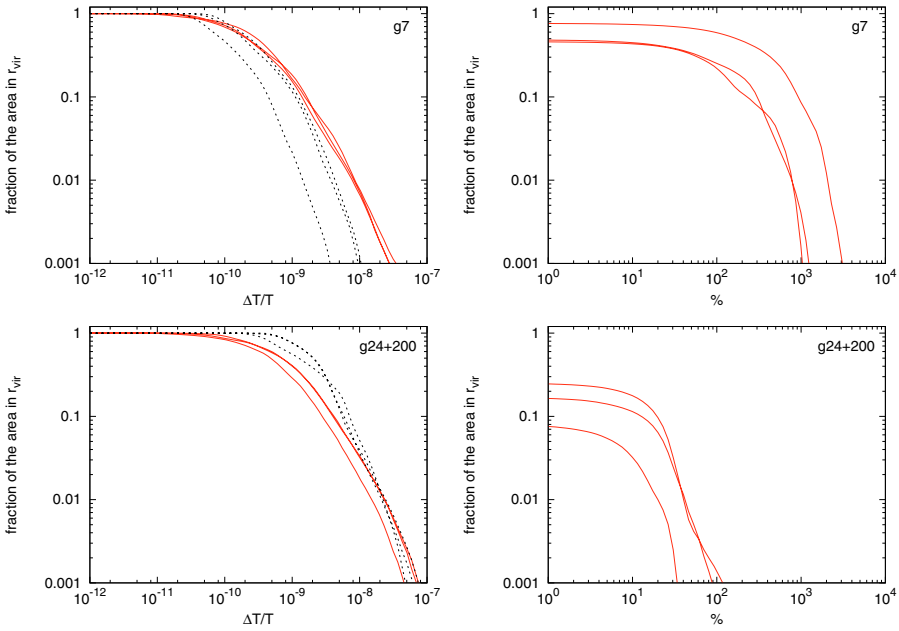

Fig. 4. The statistical distribution of the polarization signal for the merging cluster g7 (*top panels*) and for the relaxed cluster g24+200 (*bottom panels*). The results for three different Cartesian projections of each simulated cluster are shown. *The left panels* present the fraction of the virial area covered by the cluster having a polarization signal larger than a given threshold (expressed in terms of $\Delta T/T$); solid and dotted lines refer to results for the original simulations and for the "merging-free" simulations, respectively. *The right panels* show the area fraction where the per cent variation of the polarization amplification produced by the merging activity (defined as in Eq. (8)) is larger than a given threshold.

Table 1. Per cent variation of the polarization signal for clusters g7 and g24+200 placed at redshift $z = 0.1$. The table reports the values corresponding to two different area fractions (10 and 1 percent) and to four different beam resolutions (ranging from 0 to 10 arcmin).

beam	g7 (10%)	g7 (1%)	g24+200 (10%)	g24+200 (1%)
0′	550	1500	10	35
1′	490	1500	10	30
5′	480	1400	7	22
10′	477	1044	0.5	14

simulations (i.e. including the merging activity), while the dotted lines correspond to the "merging-free" simulations. A more quantitative evaluation of the differences between relaxed and un-relaxed clusters can be obtained by from the right panels, where we plot the fraction of the virial area as a function of the variation of the polarization signal produced by the merging activity. For the relaxed object g24+200 there is no significant polarization amplification from the inner dynamics: only 1 per cent of the cluster area shows an amplification of at least 30 per cent. On the contrary, the un-relaxed cluster g7 shows an increment of at least 300 per cent (800 per cent) in 10 per cent (1 per cent) of the cluster area; 50 per cent of the cluster area inside the cluster has an amplification of 50 per cent. Note that the distributions in the right panels do not reach unity, because we considered only positive variations. Thus the difference between unity and the maximum value represents the fraction of the area within the virial radius with a negative Δ: even if it may be large, we checked that it corresponds to regions where the polarization signal is negligible.

We notice that one of the three projections of cluster g7 has a significantly lower bulk velocity (379 against 577 and 624 km s^{-1}). As a consequence, in the merging-free simulation for this particular projection the polarization signal is lower, but as high as the other cases when the merging activity is fully included. This shows that the gas dynamics during the merging events dominates over the cluster bulk motion.

It is important to study how the previous results change considering different instrumental resolutions. This is evaluated by placing the galaxy clusters at redshift $z = 0.1$ and convolving the original maps with four different aperture beams. Table 1 summarizes the results obtained considering all three projections. Since the polarization signal contributed by the infalling blobs is peaked at small scales, the convolution strongly smooths the amplification produced by the merging activity. This effect is larger for lower resolutions, but it affects only the high-polarization region, leaving unchanged the signal on larger scales.

These two clusters clearly show the importance of merging activity for the polarization signal and suggests two main ways to exploit this amplification to extract useful information. First, polarization could be used to investigate the ICM dynamics. It could be possible in principle to obtain a complete three-dimensional reconstruction of the velocity field by the combination with kSZ measurements (Nagai et al. 2003): this would provide a picture of the merging history of our universe. Second, the kpSZ signal could be used to determine the tangential bulk motion of clusters, allowing a determination of the three-dimensional velocity power spectrum (always in combination with kSZ data). This would lead to independent and complementary estimates of cosmological parameters (see, e.g., Tormen et al. 1993; Moscardini et al. 1996; Bhattacharya & Kosowsky 2007). In this case the merging activity represents a strong source of noise and particular care should be taken in selecting clusters. To discuss in more detail the reliability of these two possibilities, we need to repeat the previous analysis on more robust statistical bases. For this reason we analyze the entire samples of simulated clusters in the next section.

5. Analysis of the full cluster samples

5.1. Non-radiative simulations

First, we perform a statistical analysis considering our first sample, composed of 17 different haloes simulated under the assumption of non-radiative hydrodynamics. For all objects, we consider the projections along three orthogonal lines-of-sight: this leads to 51 polarization maps. For simplicity we placed all systems at redshift $z = 0.1$.

To investigate the effect of the instrument resolution, we convolve all polarization maps with a Gaussian kernel assuming

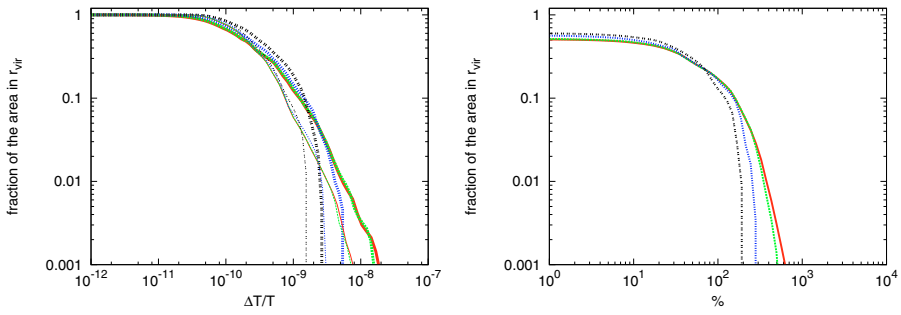

Fig. 5. The statistical distribution of the polarization signal as derived from the analysis of all projections of the 17 simulated galaxy clusters belonging to our first sample. *Left panel*: the fraction of the area having a polarization signal larger than a given threshold (expressed in terms of $\Delta T/T$); thick and thin lines refer to results for the original simulations and for the "merging-free" simulations, respectively. *Right panel*: the area fraction where the per cent amplification of the polarization signal produced by the merging activity is larger than a given threshold. Curves of different colors present the results for the original maps (red lines) and for different aperture beams: 1′ (green line), 5′ (blue line) and 10′ (black line).

different aperture beams. This is of primary importance because the largest contributions to the total signal come from small haloes, which could be smeared out by a too large beam.

In the left panel of Fig. 5 we plot the cumulative distribution of the kpSZ signal as a function of the covered area inside the virial radius. The different curves represent the median of the 51 realizations and present the results obtained from the original maps (red line) and for different aperture beams: 1′ (green line), 5′ (blue line) and 10′ (black line). The thick lines refer to the simulations including the merging activity, while the thin lines are the results for the "merging-free" simulations, i.e. where only the cluster bulk motion is accounted for. Using the same line coding, in the right panel of Fig. 5 we show the distribution of per cent amplifications for the polarization signal generated by the merging activity. As expected, the instrumental resolution causes a significant reduction of the maximum amplitude of the signal, also decreasing the increment induced by merging. The minimum aperture beam affecting the signal is obviously related to the typical scale of the objects producing the polarization peaks. This scale is ∼1 arcmin which, not surprisingly, is of the same order as the halo core radius ($r_c \sim 0.11\ h^{-1}$ Mpc at $z = 0.1$).

Our results suggest that the upcoming millimetric observatories, having angular resolutions of the order of $FWHM \simeq 1'$ or better, will be sensitive to the merging activity of galaxy clusters, which is expected to amplify the kpSZ signal by a factor of about 5 over at least 1 percent of the virial area. The plot also shows that on average the cluster population has a maximum signal of $\Delta T/T \approx 10^{-8}$, while merging systems have peaks up to 10^{-7}: this confirms what we obtained from the analysis of two clusters g7 and g24+200 in the previous section.

We notice that this median distribution, which represents the typical expectation for the composite cluster population including both relaxed and non-relaxed objects, is consistent with the results obtained by Lavaux et al. (2004). However we point out that the merging clusters may have a kpSZ signal that is 10 times stronger.

Additionally to the dynamic information carried by this effect, the kpSZ effect can become a non-negligible source of noise in the estimateion of the CMB quadrupole when observing the polarization induced by the intrinsic CMB quadrupole P_Q. This makes it necessary both to have access to a component-separation technique based on multi-frequency observations and to carefully choose the clusters to be considered, which should be as relaxed as possible. This selection can be performed with X-ray and SZ observations.

5.2. Effects of ICM modeling

We analyze the second simulation set to investigate the effects of different ICM modeling on the statistical properties of the kpSZ signal. Again, the 9 objects were projected in 3 different orthogonal directions, leading to 27 polarization maps for each of the ICM models described in Sect. 3.

As an example, we shown in Fig. 6 the polarization maps for the unrelaxed cluster g51 as obtained using the same projection, but with the inclusion of different physical processes. This object has a mass of $\approx 1.3 \times 10^{15}\ h^{-1}\ M_\odot$ and a virial radius of $\approx 2.3\ h^{-1}$ Mpc (corresponding to the circle in the plot). The properties of the large-scale polarization signal, coming from diffuse structures, are similar in the different panels, reaching values of the order of ∼1 nk. We find significant changes only in the most central regions of the cluster, where the different ICM modeling plays an important role. In particular, from the comparison of the two upper panels, it is evident that the *ovisc* and *lvisc* models give almost equivalent kpSZ signals, with consistent maximum amplitudes (967 nk and 1123 nk, respectively). Also the different features present in the map have coincident positions and very similar appearence (they are only slightly smoother in the *ovisc* model). Since the only difference in the ICM modeling implemented in these two simulations is the possibility of better resolving the turbulent motion driven by fluid instabilities in the *lvisc* model, our results suggest that their relevance for polarization is negligible. The processes of cooling, star formation and supernova feedback with weak winds which are active in the *csf* simulation, smear out the highest peaks in the cluster core, strongly reducing the maximum signal (285 nk), almost half an order of magnitude smaller than in the previous cases. The general properties of the polarization signal in the *csfc* model are similar to the *csf* case, with the exception that at the small scales, the signal is slightly smoothed by thermal conduction.

In Fig. 7 we show the polarization maps, but for the more relaxed and smaller cluster g6212 (having a virial mass and radius of $\approx 1.15 \times 10^{14}\ h^{-1}\ M_\odot$ and $\approx 1.0\ h^{-1}$ Mpc, respectively). In this case the kpSZ signal comes only from the most internal regions (one third of the virial radius) with peaks up to a few tens of μK. Again the maps for the two non-radiative simulations are very similar, with no significant difference between the *ovisc* and *lvisc* models. For the simulations including cooling, star formation and feedback, the typical values of $\Delta T/T$ at the centre are smaller. The reduction is particularly evident for the *csfc* model: unlike for the cluster g51, in the case of g6212, given its smaller mass, the thermal conduction is more efficient in smoothing the signal. Comparing the results shown in Figs. 6 and 7, we find

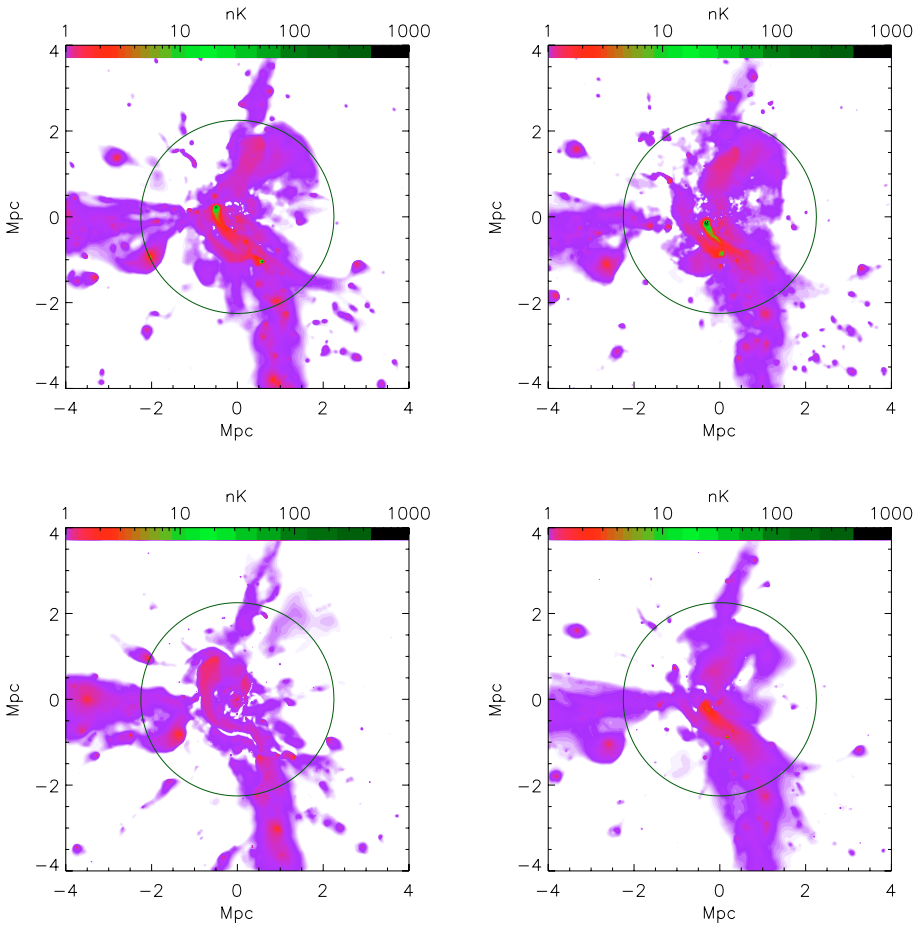

Fig. 6. Maps for the polarization signal for the same cluster, g51, but simulated with different ICM modeling: *ovisc* (*top left*), *lvisc* (*top right*), *csf* (*bottom left*), *csfc* (*bottom right*). The same projection is shown in all panels; the circle represents the virial radius.

that, as expected, the different ICM modeling has larger effects on smaller clusters. However, this tendency is partially counterbalanced by the fact that the kpSZ signal mostly comes from the cluster core and low-mass clusters are more concentrated than high-mass systems.

A more quantitative picture can be drawn considering the statistical properties of the total sample. In Fig. 8 we show the distributions of polarization amplitude for each of the four ICM models considered here. In particular the curves represent the median of the 27 maps and refer to the differential and cumulative distributions (left and right panels). As previously pointed out, the differences between the *ovisc* and *lvisc* models are negligible. The radiative processes acting in the *csf* model produce some changes, mostly in the high-signal tail, where the polarization amplitude is reduced by at most a factor of 2. A further small signal reduction is given by the switching on of the thermal conduction in the *cfsc* model. However, these differences involve only a few per cent of the total cluster area.

6. Conclusions

We measured the dynamics of the ICM during galaxy cluster mergers using the kinematic Sunyaev-Zel'dovich polarization (kpSZ) induced on the CMB (Sunyaev & Zel'dovich 1980a; Sazonov & Sunyaev 1999). This effect is caused by the single scattering of moving electrons: its dependence on the square of the tangential electron velocity makes it a suitable probe to investigate the kinematic properties of forming cosmic structures.

We used the outputs of 53 high-resolution hydrodynamical *N*-body simulations to create realistic maps for this observable, which have been statistically analysed, focusing on the polarization signal induced by in-falling blobs. We demonstrated that the amplitude of the cluster signal can vary by up to one order of magnitude depending on the internal cluster dynamics.

We found that the median kpSZ signal of the whole population is about 10^{-8} K, which could be observed by upcoming millimetric observatories. In addition we showed that major merger events in unrelaxed clusters can produce a polarization amplification of one order of magnitude, with values up to 10^{-7} K. These high peaks in the kpSZ signal are however related to fast in-falling blobs, corresponding to small angular scales: consequently, high instrumental resolution (i.e. a small aperture beam) is fundamental to avoid smearing out the signal.

The main difficulty to significantly detect the polarization signal from clusters is related to the availability of future high-sensitivity and high-resolution instruments able to measure the polarization of CMB photons. This level of accuracy will be approached by the next generation of millimetric observatories, such as, for example, Polarbear-II[3] ($FWHM = 4$ arcmin and $\Delta T/T = 2.5\ \mu$K) or Polatron ($FWHM = 2.5$ arcmin and $\Delta T/T = 6\ \mu$K, Philhour et al. 2001).

Nevertheless our results show that the merging activity is of fundamental importance to estimate the three-dimensional velocity power spectrum of non-linear structure through the observations of the kpSZ and SZ signals. The amplification given by internal motion could be dominant with respect to the signal generated by the bulk velocity of clusters, resulting in a non-negligible source of noise for such measurements. This is also true for the estimation of the CMB quadrupole from the observation of the polarization induced by the intrinsic CMB

[3] bolo.berkeley.edu/polarbear/

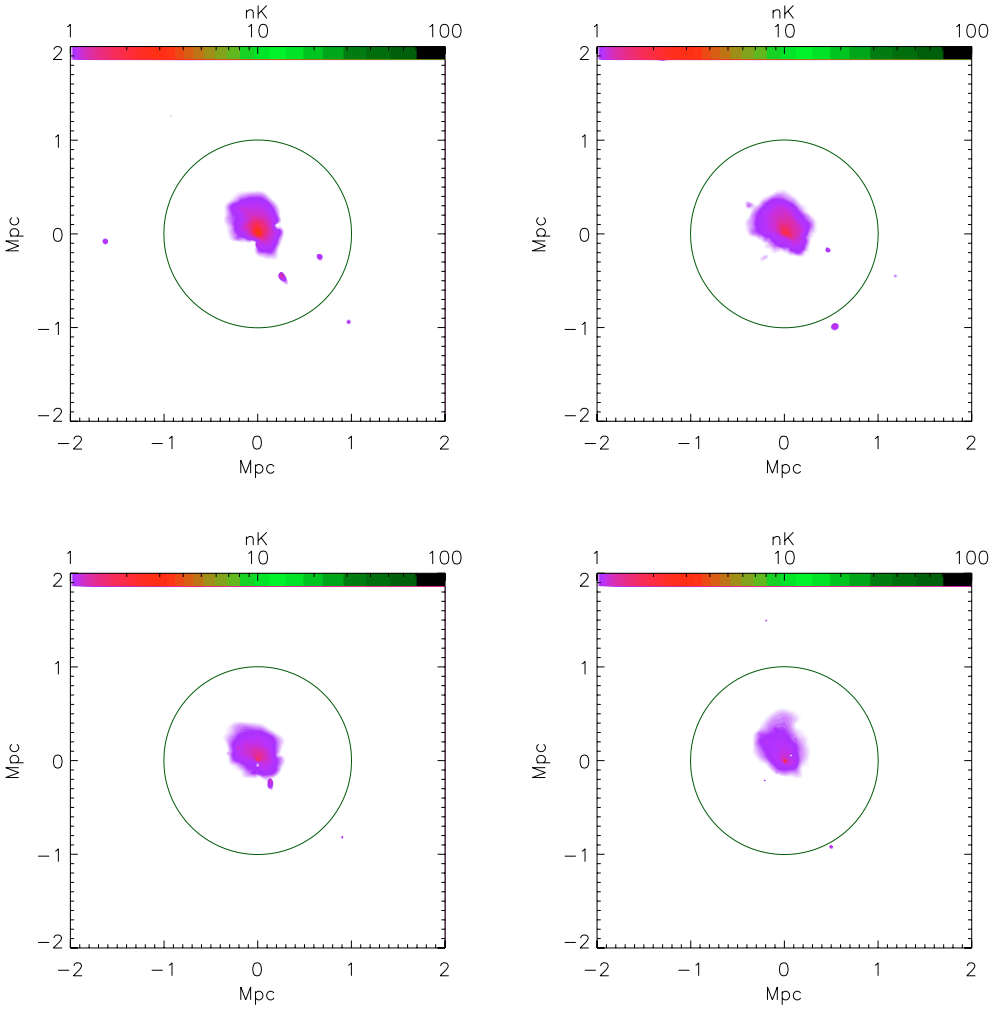

Fig. 7. As Fig. 6, but for the more relaxed and smaller cluster g6212.

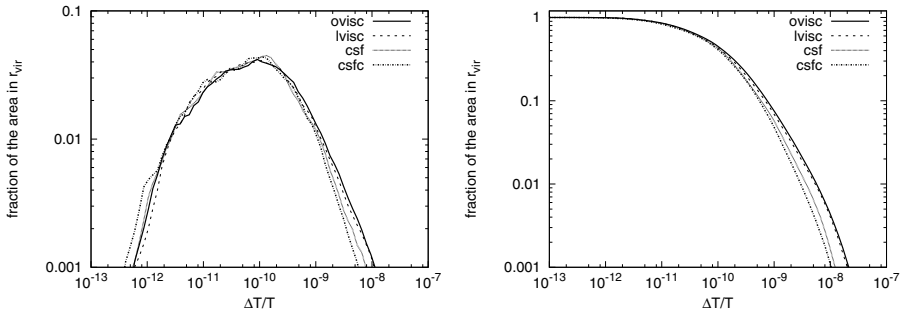

Fig. 8. The differential (*left panel*) and cumulative (*right panel*) distributions of the polarization signal, as measured using all projections of the 9 simulated galaxy clusters belonging to our second sample. The different lines refer to results for simulations with different ICM modeling, as indicated in the panels.

quadrupole P_Q. This makes necessary both a robust component separation based on multi-frequency observations and a careful selection of the clusters to be observed, which should be as relaxed as possible.

Acknowledgements. Computations have been performed using the IBM-SP4/5 at CINECA (Consorzio Interuniversitario del Nord-Est per il Calcolo Automatico), Bologna, with CPU time assigned under an INAF-CINECA grant. We acknowledge financial contribution from contract ASI-INAF I/023/05/0 and INFN PD51. We thank Massimo Meneghetti and Daniele Dallacasa for useful discussions.

References

Allen, S. W., Fabian, A. C., Johnstone, R. M., Arnaud, K. A., & Nulsen, P. E. J. 2001, MNRAS, 322, 589
Amblard, A., & White, M. 2005, New Astron., 10, 417
Bhattacharya, S., & Kosowsky, A. 2007, ApJ, 659, L83
Burigana, C., La Porta, L., Reich, P., & Reich, W. 2006, Astron. Nachr., 327, 491
Diego, J. M., Mazzotta, P., & Silk, J. 2003, ApJ, 597, L1
Dolag, K., Jubelgas, M., Springel, V., Borgani, S., & Rasia, E. 2004, ApJ, 606, L97
Dolag, K., Vazza, F., Brunetti, G., & Tormen, G. 2005, MNRAS, 364, 753
Eke, V. R., Cole, S., & Frenk, C. S. 1996, MNRAS, 282, 263
Ettori, S., Dolag, K., Borgani, S., & Murante, G. 2006, MNRAS, 365, 1021

Hu, W. 2001, ApJ, 557, L79
Hu, W., DeDeo, S., & Vale, C. 2007, preprint [arXiv:astro-ph/0701276]
Jubelgas, M., Springel, V., & Dolag, K. 2004, MNRAS, 351, 423
Lavaux, G., Diego, J. M., Mathis, H., & Silk, J. 2004, MNRAS, 347, 729
Liu, G.-C., da Silva, A., & Aghanim, N. 2005, ApJ, 621, 15
Maturi, M., Bartelmann, M., Meneghetti, M., & Moscardini, L. 2005, A&A, 436, 37
Moscardini, L., Branchini, E., Brunozzi, P. T., et al. 1996, MNRAS, 282, 384
Nagai, D., Kravtsov, A. V., & Kosowsky, A. 2003, ApJ, 587, 524
Ng, K. L., & Ng, K.-W. 1996, ApJ, 456, 413
Ohno, H., Takada, M., Dolag, K., Bartelmann, M., & Sugiyama, N. 2003, ApJ, 584, 599
Page, L., Hinshaw, G., Komatsu, E., et al. 2007, ApJS, 170, 335
Philhour, B. J., Keating, B. G., Ade, P. A. R., et al. 2006, preprint [arXiv:astro-ph/0106543]
Rasia, E., Tormen, G., & Moscardini, L. 2004, MNRAS, 351, 237
Roncarelli, M., Ettori, S., Dolag, K., et al. 2006, MNRAS, 373, 1339
Sazonov, S. Y., & Sunyaev, R. A. 1999, MNRAS, 310, 765
Shimon, M., Rephaeli, Y., O'Shea, B. W., & Norman, M. L. 2006, MNRAS, 368, 511
Springel, V. 2005, MNRAS, 364, 1105
Springel, V., & Hernquist, L. 2002, MNRAS, 333, 649
Springel, V., Yoshida, N., & White, S. 2001, New Astron., 6, 79
Sunyaev, R., & Zel'dovich, I. 1980a, ARA&A, 18, 537
Sunyaev, R. A., & Zel'dovich, I. B. 1980b, MNRAS, 190, 413
Tegmark, M., Eisenstein, D., Hu, W., & de Oliveira-Costa, A. 2000, ApJ, 530, 133
Tegmark, M., de Oliveira-Costa, A., & Hamilton, A. J. 2003, Phys. Rev. D, 68, 123523
Tormen, G., Moscardini, L., Lucchin, F., & Matarrese, S. 1993, ApJ, 411, 16
Tormen, G., Bouchet, F. R., & White, S. D. M. 1997, MNRAS, 286, 865
Tormen, G., Moscardini, L., & Yoshida, N. 2004, MNRAS, 350, 1397
Yoshida, N., Sheth, R., & Diaferio, A. 2001, MNRAS, 328, 669
Zaldarriaga, M., & Seljak, U. C. V. 1998, Phys. Rev. D, 58, 023003